Implementation and Verification of the SCattering Index: An Extension of UV Aerosol Index from GOME-2

Final report of the visiting scientist at KNMI
April 2012

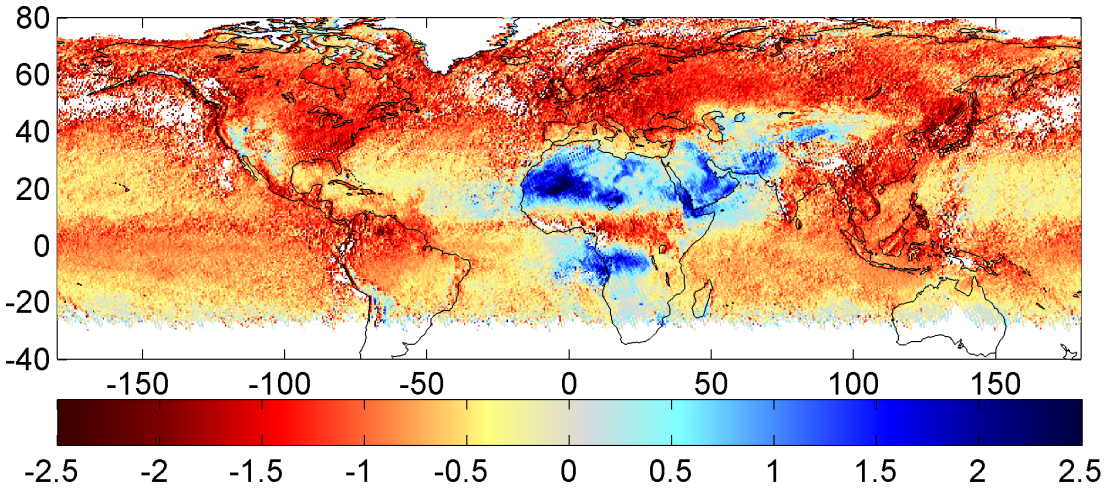

Figure 0. Degradation-corrected GOME-2 Aerosol Indices (HICRU cloud fraction < 0.2) for July, 2011. Blue tones indicate absorbing aerosols; red/yellow tones indicate scattering (non-absorbing) aerosols and remaining clouds.

Authors: Marloes Penning de Vries, Gijsbert Tilstra, Olaf Tuinder, Michael Grzegorski, Thomas Wagner, Piet Stammes

Contents

1. Summary 2

2. Introduction 3

3. SCattering Index (SCI) 4
   3.1. Comparison with AERONET and MODIS AOT: Southeast Asia 4
   3.2. UVAI inter-comparison (OMI, SCIAMACHY, and GOME-2): Sulphate aerosols from Mount Kilauea 8

4. HICRU 12
   4.1. Short description of HICRU 12
   4.2. Validation of HICRU for GOME-2 with FRESCO+ 13

5. Conclusions and recommendations 17

6. Acknowledgments 18

7. References 18

8. Abbreviations 19

Appendix 1. Project overview and time schedule 20

1. Summary

The main purpose of our visiting scientist project was the implementation of the SCattering Index (SCI) for GOME-2 as a counterpart to the existing Absorbing Aerosol Index (AAI). After implementation, the SCI was verified by comparison with Aerosol Optical Thickness (AOT) from satellite-borne MODIS and ground-based AERONET measurements. Monthly averaged quantities are found to be in agreement for many cases. The presented cases clearly illustrate the two main advantages of SCI and AAI: (1) they contain aerosol information even in the presence of clouds; (2) taken together, they provide information on aerosol absorption without requiring assumptions on aerosol type. Nevertheless, the indices SCI and AAI should be interpreted with caution: we recommend using averaged values, preferably in combination with AOT data from, e.g., MODIS.

The indices SCI and AAI are influenced by clouds; therefore it is of importance to have a collocated cloud product of good quality. For this reason, we implemented a prototype version of the HICRU effective cloud fraction retrieval algorithm. HICRU uses reflectances from a GOME-2 PMD channel as input, providing a cloud product with eight times higher spatial resolution than, e.g., FRESCO+. In addition, the HICRU algorithm applies image sequence analysis to determine clear-sky reflectances instead of relying on a surface albedo database. The agreement between HICRU and FRESCO+ effective cloud fractions for one month of data is excellent when the difference in cloud models is taken into account. This leads us to the conclusion that the implementation of the HICRU prototype was successful.

2. Introduction

The retrieval of aerosol optical properties using space-based instruments is not a trivial task, mostly because of three complications: varying surface albedo, cloud contamination, and the large variety in aerosol types. Currently, there is no single satellite instrument capable of retrieving all aerosol properties simultaneously, let alone in the presence of clouds, and the focus of most satellite aerosol retrievals is on Aerosol Optical Thickness (AOT). The UV Aerosol Indices (UVAI) are semi-quantitative indicators of aerosol absorption [Herman et al., 1997; Torres et al., 1998] and thus add complimentary information to AOT measurements. They are relatively insensitive to surface type and can be (and are) determined even in scenes containing clouds.

There are two sides to the UVAI: the Absorbing Aerosol Index (AAI), traditionally used to detect biomass burning smoke, elevated plumes of mineral dust, and volcanic ash clouds (see, e.g. [de Graaf et al., 2005; de Graaf, 2006] and references therein). And the SCattering Index (SCI), which is indicative of scattering aerosols, such as sulphate droplets and secondary organic aerosols, but which is also sensitive to clouds [Penning de Vries et al., 2009]. Although the UVAI cannot be simply used in a quantitative sense (like, e.g., AOT), information on aerosol absorption is very valuable to radiative forcing studies or for the characterisation of aerosol types. UVAI have been calculated from UV reflectances since the first TOMS instrument (1978) and are currently available for GOME, SCIAMACHY, OMI, and GOME-2, constituting a long, nearly unbroken global record of aerosol absorption.

For the correct interpretation of UVAI it is of importance to have accurate cloud data, as UVAI depend on cloud fraction [Penning de Vries et al., 2009; Penning de Vries and Wagner, 2011]. Similar to aerosol retrieval, the retrieval of clouds requires a good knowledge of the surface albedo. The HICRU Iterative Cloud Retrieval Utilities (HICRU) algorithm uses image sequence analysis of the dataset itself to construct a map of reflectances of cloud-free scenes, which is then used for cloud fraction retrieval [Grzegorski et al., 2006]. The spatial resolution of HICRU cloud fractions is higher than for the science channel products (such as UVAI) because the reflectances that are used in the algorithm are obtained by the instrument's polarisation measurement devices (PMDs). This makes HICRU very suitable for use with other (future) PMD products, such as AOT or UVAI.

This document is structured as follows: section 3 presents the work we performed on the implementation and verification of SCI. In section 4, we shortly explain the HICRU algorithm and show a comparison with cloud fractions obtained using the FRESCO+ algorithm. Section 5 contains our conclusions and recommendations. An overview of the project and the time plan can be found in Appendix 1.

3. SCattering Index (SCI)

The implementation of SCI has been completed by the inclusion of negative values for the GOME-2 UV Aerosol Index product. A complete view of the UV Aerosol Index is shown on the title page of this document (Fig. 0), with a colour scale chosen to emphasize the SCI. The data shown in Fig. 0 are an average of July, 2011, and were cloud-filtered by requiring that the HICRU cloud fraction < 0.20. Additionally, data were selected by solar zenith angle (smaller than 60°) and scattering angle (larger than 90°) and freed of backscans, orbits in narrow swath or nadir static mode, and pixels in sun glint geometry. Gaps in the dataset, caused by the stringent filtering, show up in white in Fig. 0. The most prominent features are mineral dust and biomass burning smoke, which absorb UV radiation and cause positive UVAI (non-zero AAI, shown in blue in Fig. 0). Most of the Northern Hemisphere is seen to be affected by non-absorbing aerosols (in particular in the eastern U.S., most of Europe, and Southeast Asia), but part of that SCI signal (in yellow-red tones) can be attributed to residual clouds. The information content of SCI is the topic of the following Sections 3.1 and 3.2.

It is known that the GOME-2 UV channels are degrading rapidly and that the UVAI is strongly affected: the global average has decreased from about -0.5 in 2007 to -2 at the end of 2011 at nadir. In addition, a strongly viewing-angle dependent component causes the difference in global average UVAI between the pixels on the eastern and western swath edges to increase to 3 units (in December, 2011), up from 1 unit (in January, 2007) [Tilstra et al., 2012a]. We removed the effects of degradation by using a first-order, empirical correction on the Aerosol Index that was developed by G. Tilstra. It is based on the assumption that the global average UVAI is constant (see also [Tilstra et al., 2012b]) and is a simple subtraction of a correction term given by the deviation of global average UVAI from the global average UVAI at the beginning of the mission as a function of time and viewing angle.

Below, we provide some representative results from an extensive verification study of SCI and AAI with AOT from MODIS [Remer et al., 2008] and level-2 AOT from AERONET [Holben et al., 1998].

3.1. Comparison with AERONET and MODIS AOT: Southeast Asia

We compared AOT from seven ground-based AERONET stations in Southeast Asia with AOT from MODIS and degradation-corrected GOME-2 UVAI for the time range 2007-2010. The two examples shown below give a good indication of the strengths and weaknesses of UVAI.

In Fig. 1, the average AOT (panel A) and UVAI (panel B) are shown for Southeast Asia in March, 2007. MODIS AOT data are missing for large parts of the scene due to persistent clouds or snow- and ice-covered surfaces, but it can be seen that the average aerosol load over Southeast Asia is very high (with $AOT_{550} > 1$, especially along the East coast of China). In March, the aerosols in the regions under study (white boxes, marked “N” and “S” for “north” and “south”, respectively) are mostly absorbing aerosols: mineral dust transported from Mongolia and the Taklimakan desert in the north, and smoke from agricultural waste burning in the south. This is clearly seen in the GOME-2 UVAI, where the absorbing aerosols show up in blue. Please note that no cloud filter was applied to the GOME-2 data.

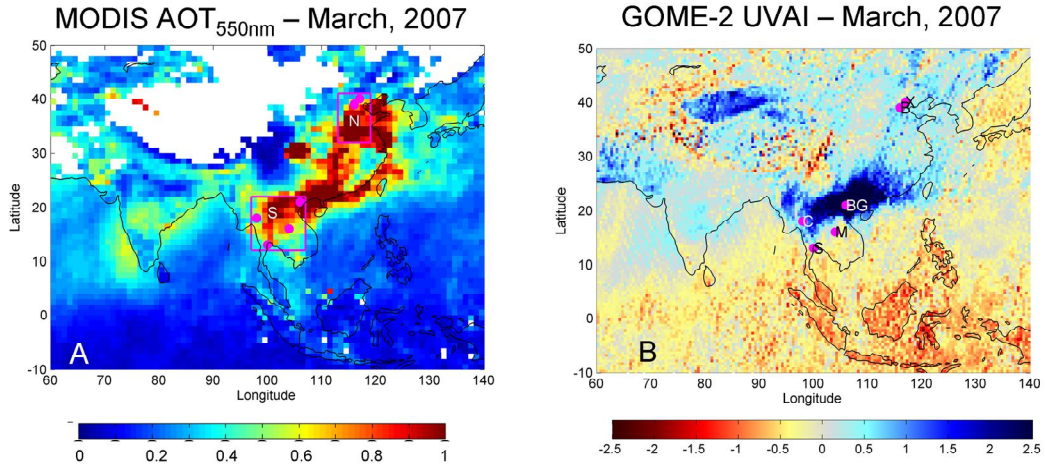

Figure 1. Monthly averages of aerosol abundance for March, 2007. A, MODIS AOT (550 nm) averaged on a 1°x1° grid. B, GOME-2 UV Aerosol Index on a 0.5°x0.5° grid. No cloud filter was applied to the GOME-2 data. The boxes, marked "N" and "S", respectively indicate the northern and southern regions used for SCI verification. The dots mark the AERONET stations: X, Xinglong (China), B, Beijing and XiangHe (China), BG, BacGiang (Vietnam), C, ChiangMai (Thailand), M, Mukdahan (Thailand), S, Silpakorn (Thailand).

To study the seasonal cycle of aerosols in Southeast Asia in a more quantitative sense, the aerosol abundance (AOT and UVAI) in the white boxes in Fig. 1A were integrated for each month from 2007-2010. The results for box "S" are shown in Fig. 2A and 2B respectively, together with the averaged MODIS fine-mode fraction (panel D) and the monthly averaged level-2 AOT from the four AERONET stations within box "S" (panel C). The fine-mode fraction (FMF) is the relative weighting of a "coarse" (effective particle radius > 1 µm) and a "fine" aerosol model (effective radius < 1 µm) used in the MODIS AOT retrieval and, as such, is an indication of particle size. The data depicted in Fig. 2D and following figures (4D and 6C) were obtained by weighting the monthly average FMF in each grid box with the average AOT in the corresponding grid box before integrating over the region of interest.
Both AOT datasets, MODIS and AERONET, show pronounced maxima in March and October of every year (vertical bars in each panel). The maximum in March is caused by smoke from agricultural fires, as mentioned above, and matches the observed UVAI maximum. In October, the high AOT is caused by a mixture of aerosols originating from biogenic and industrial emissions. This second AOT maximum is matched by a minimum in UVAI – a maximum in SCI – indicating that these aerosols absorb no or little UV radiation.
The fine-mode fraction peaks at the AOT maxima, indicating that the aerosols are small. The peak value of about 0.7, however, shows that there is also a significant coarse-mode aerosol fraction present.

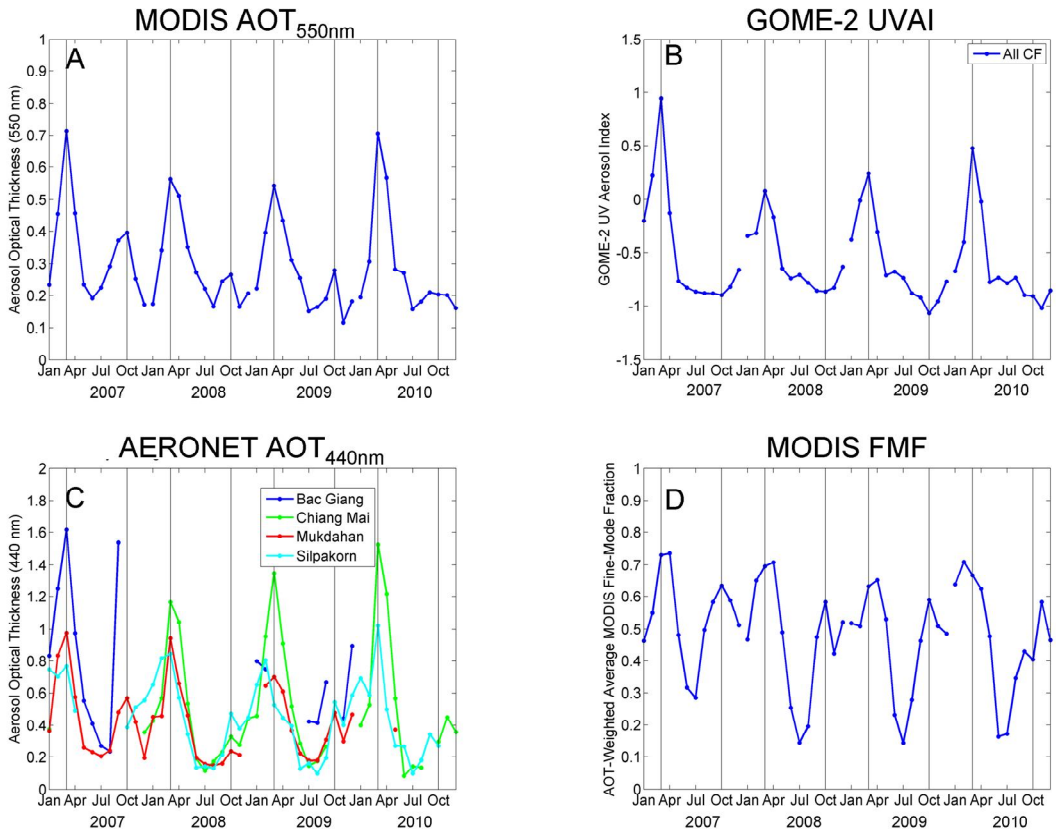

Figure 2. Time series of monthly averaged aerosol abundance and fine-mode fraction for box "S" in Fig. 1 (Thailand and Vietnam). A, MODIS AOT (550 nm); B, GOME-2 UV Aerosol Index (no cloud filter); C, AERONET AOT (440 nm) for selected stations depicted in Fig. 1; D, MODIS FMF. Vertical lines indicate AOT maxima in March and October.

Similar to Fig. 1, in Fig. 3 the average AOT (panel A) and UVAI (panel B) are plotted for Southeast Asia, but now for June, 2007. Again, MODIS AOT shows that the aerosol load is very high in the region. From the UVAI plot it can be seen that whereas most of the aerosols in the South of the depicted region do not absorb UV radiation (negative UVAI), the North is affected by UV-absorbing mineral dust that is transported from Mongolia and the Taklimakan Desert to the East coast of China (positive UVAI). The Indo-Gangetic Plains (South of the Tibetan plateau) are affected by a mixture of smoke, dust, and other polluting aerosols leading to very high AOT in this season. GOME-2 UVAI shows that these aerosols are mostly UV-absorbing particles.

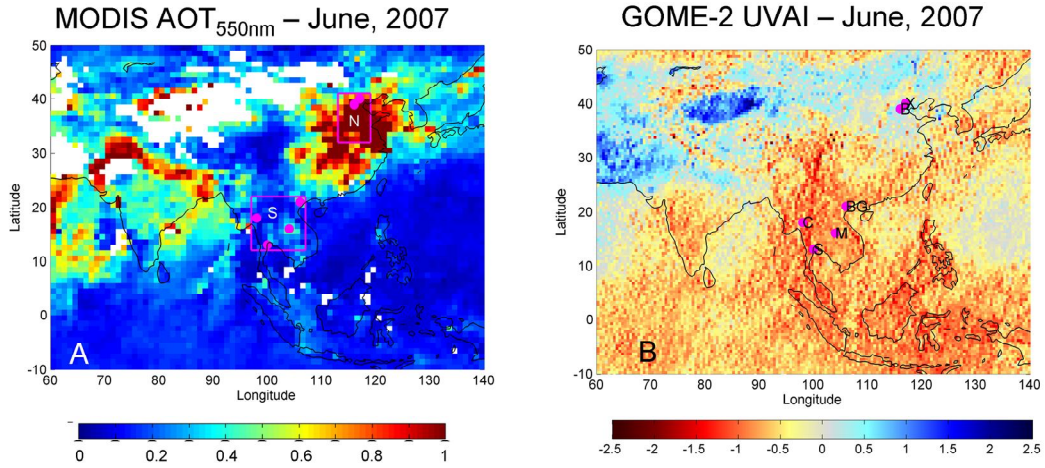

Figure 3. Monthly averages of aerosol abundance for June, 2007. A, MODIS AOT (550 nm) averaged on a 1°x1° grid. B, GOME-2 UV Aerosol Index on a 0.5°x0.5° grid. No cloud filter was applied to the GOME-2 data. The boxes, marked "N" and "S", respectively indicate the northern and southern regions used for SCI verification. The dots mark the AERONET stations: X, Xinglong (China), B, Beijing and XiangHe (China), BG, BacGiang (Vietnam), C, ChiangMai (Thailand), M, Mukdahan (Thailand), S, Silpakorn (Thailand).

The time series of aerosol abundance and fine-mode fraction, as determined for box "N" in Figs. 1 and 3, is presented in Fig. 4. MODIS and AERONET AOT both display a clear maximum in June (panels A and C, respectively), which is found neither in the UVAI, nor in the FMF time series. Instead, UVAI and FMF both peak two months later, in August. This discrepancy is probably due to the particular mix of aerosol types in the studied region: in spring, Beijing is often affected by mineral dust from the surrounding deserts, which consists of large particles (hence the low FMF) that absorb UV radiation (positive UVAI). During summer, from June to August, the high AOT is dominated by small, non-absorbing aerosol particles (high FMF, negative UVAI), which are almost certainly of anthropogenic origin (industry and other urban emissions).

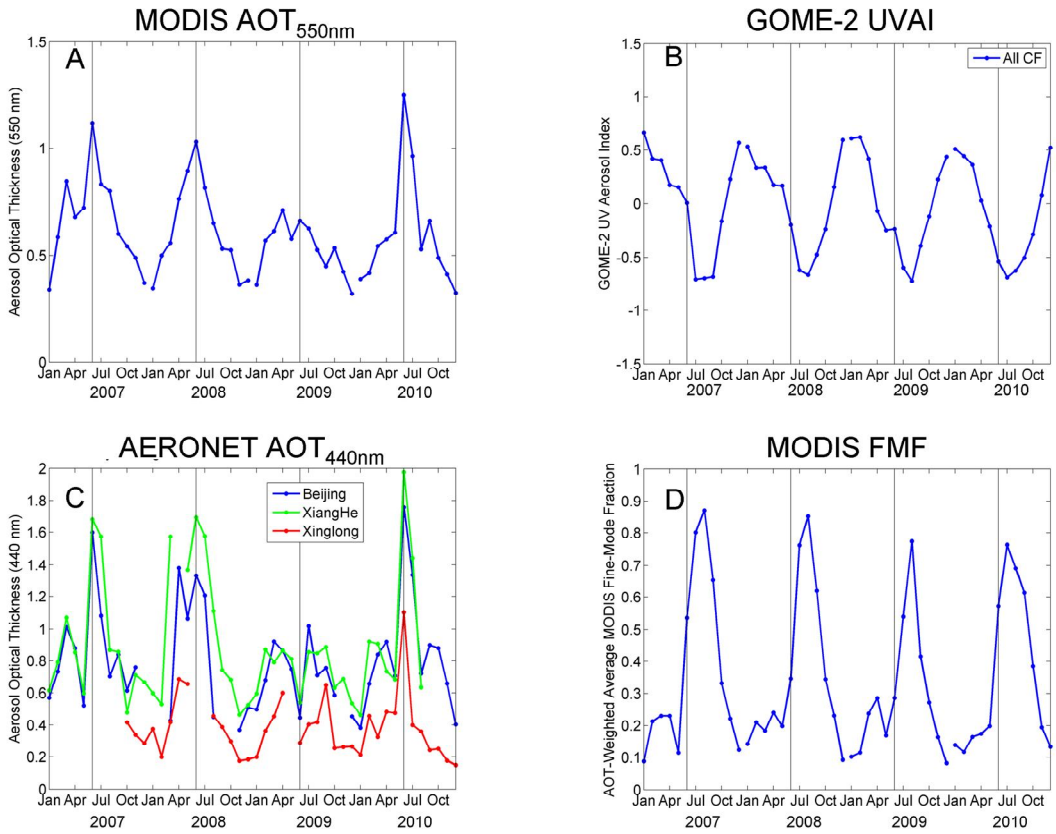

Figure 4. Time series of monthly averaged aerosol abundance and fine-mode fraction for the box "N" in Figs. 1 and 3 (Beijing region). A, MODIS AOT (550 nm); B, GOME-2 UV Aerosol Index (no cloud filter); C, AERONET AOT (440 nm) for selected stations depicted in Figs. 1 and 2; D, MODIS FMF. Vertical lines indicate AOT maximum in June.

These examples demonstrate the strengths of UVAI: (1) the possibility of detecting aerosols in the presence of clouds, and (2) distinguishing between absorbing and non-absorbing aerosols without assumptions on aerosol type. This provides us with additional, independent information on aerosol optical properties that, in conjunction with, e.g., MODIS AOT can be used for more accurate aerosol characterisation.
Some UVAI weaknesses also become apparent: (1) many factors apart from aerosols cause non-zero UVAI, and (2) zero UVAI does not necessarily mean that there are no aerosols; mixtures of absorbing and non-absorbing aerosols may cause positive and negative UVAI to cancel out. It is therefore advised to use the UVAI in combination with auxiliary data that show the presence of aerosols with more confidence (e.g., AOT).

3.2 UVAI inter-comparison (OMI, SCIAMACHY and GOME-2): Sulphate aerosols from Mount Kilauea

The prolonged continuous degassing of Mt. Kilauea on Hawaii in 2008 provided us with an ideal case for the verification of SCI. The extensive plume was located over ocean and remained very constant, which allowed for the study of monthly averages, decreasing the

noise in the GOME-2 data. In addition, the islands of Hawaii are very remote and the region is not polluted by aerosols from continental sources.
Figure 5 shows the monthly average AOT measured by MODIS (left) and UVAI from GOME-2 (right) for August, 2008 (top panels). The plume, consisting mostly of sulphate droplets, can be clearly seen to stretch over a length of several thousands of kilometres. As a reference, monthly average AOT (left) and UVAI (right) are also shown for August 2007, when there was significantly less degassing by Hawaiian volcanoes.

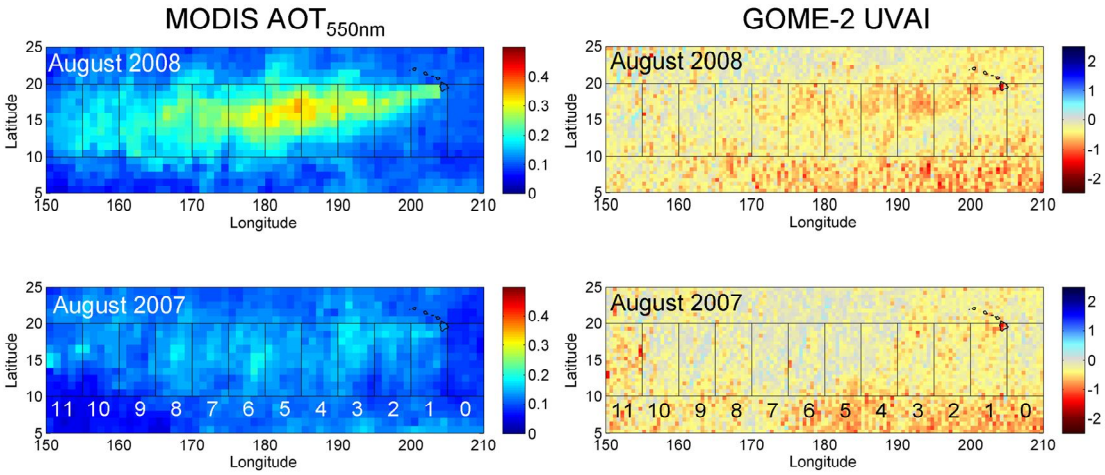

Figure 5. Monthly averages of aerosol abundance for August, 2008 (upper row) and August, 2007 (reference year, lower row). Left, MODIS AOT (550 nm) averaged on a 1°x1° grid. Right, GOME-2 UV Aerosol Index on a 0.5°x0.5° grid. No cloud filter was applied to the GOME-2 data. The boxes indicate the regions used for the SCI verification shown in Fig. 6.

There is a clear signal of the sulphate aerosols in the UVAI data, although it is not as easily discernable as in the case of MODIS AOT. The fact that no positive UVAI values are found is a strong indication that no significant amounts of UV-absorbing ash were present. In the panel with UVAI for the reference year 2007 it can be seen that there are a lot of contributions from other sources than aerosols: most of it is probably attributable to clouds, but ocean colour and whitecaps may also play a role.
On comparing the two top panels of Fig. 5, it can be seen that the AOT plume shape is quite different from the UVAI plume shape. This may have to do with the fact that MODIS AOT measurements are performed for strictly cloud-free pixels only, whereas the GOME-2 UVAI data in Fig. 5 were not cloud-filtered. In addition, the two algorithms are sensitive to different aspects of aerosol scattering: MODIS AOT is sensitive to the reflectance increase (at 550 nm) caused by sulphate aerosols, which increases with aerosol particle size. In contrast, GOME-2 UVAI is most sensitive to the spectral dependence of aerosol scattering, which decreases with increasing particle size. In contrast to AAI, SCI is not sensitive to aerosol altitude.
A more detailed study of the sulphate aerosol plume was performed by dividing the region between 10°N and 20°N into twelve sections (boxes in Fig. 5) of 5° width each. The width of one box corresponds approximately to the distance travelled by the plume in one day.

The box labelled "0" lies upwind of the volcano and contains no significant amount of sulphate aerosols. Figure 6 shows the integrated aerosol abundance (and fine-mode fraction) for each of the boxes. Please note that panels B and D in Fig. 6 display SCI, not UVAI, to facilitate the comparison with MODIS AOT.

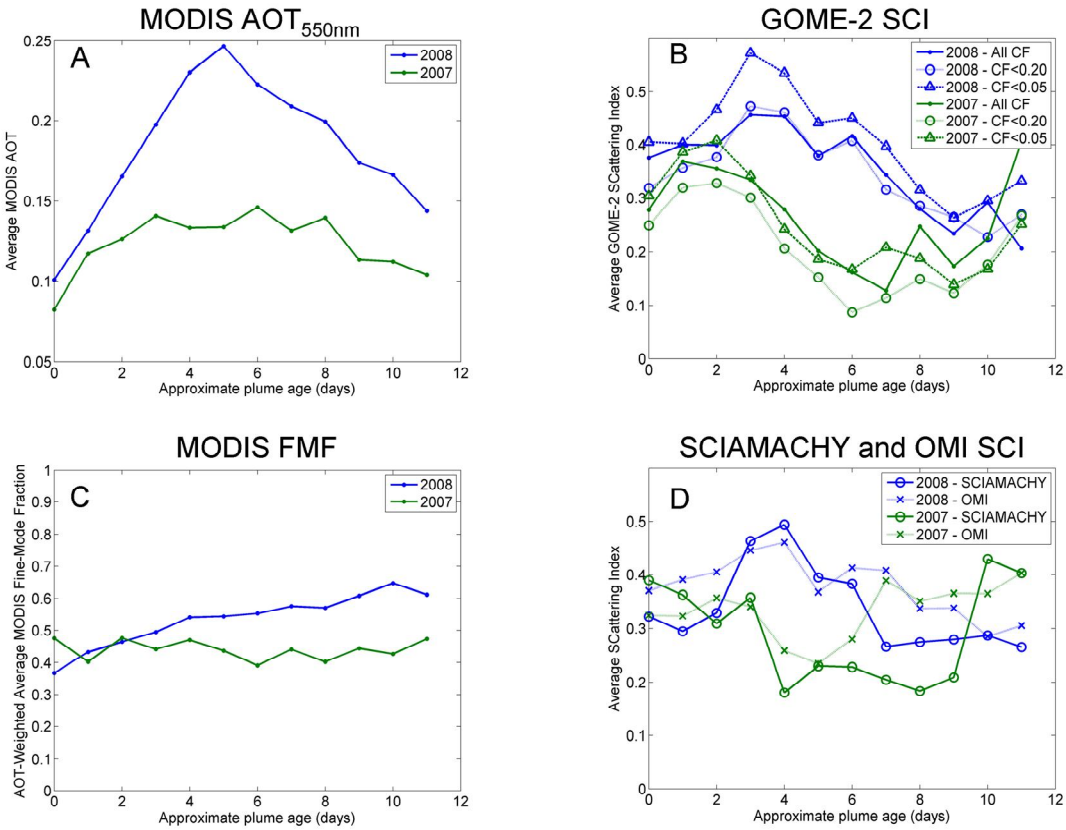

Figure 6. Time series of monthly averaged aerosol abundance and fine-mode fraction for the boxes depicted in Fig. 5; the numbers on the x-axis correspond to the box labels in Fig. 5. A, MODIS AOT (550 nm); B, GOME-2 SCattering Index; C, MODIS FMF; D, SCIAMACHY and OMI SCattering Index. Data shown are monthly averages for August, 2008 in blue, and August, 2007 as a reference in green. GOME-2 SCI averages were computed without (solid lines and dots) and with two different cloud filters, as given in the legend and the text. No cloud filter was applied to the SCIAMACHY and OMI data.

In panel A of Fig. 6, the AOT of the sulphate aerosol plume can be clearly seen to increase with plume age, reach a maximum after five days, and decline again nearly to background levels after eleven days. As mentioned above, the plume shape appears different in the GOME-2 and SCIAMACHY SCI data (panels B and D): the maximum appears earlier (days 3-4) and the SCI returns to background levels more quickly (days 7-8). In the OMI SCI the plume is difficult to make out; possibly because of an increase in background signal (the reference year 2007 shows an increase in SCI at 6-7 days). We investigated the impact of a cloud filter on the plume shape using FRESCO+ effective cloud fraction (HICRU data are not yet available for this dataset). Removing cloudy pixels from the GOME-2 SCI data using different cloud filters (CF<0.20 and CF<0.05) does not have a large impact on the plume shape, although the SCI detected by GOME-2 is larger when the strictest cloud filter

(CF<0.05) is applied. The MODIS cloud retrieval works on much smaller spatial scales than GOME-2, on the order of 1 km, which may affect the plume shape despite the fact that we found no effect upon filtering of the GOME-2 data.

One reason that the observed SCI is not very sensitive to the plume under study (in comparison to MODIS AOT) may be found in the lower left plot in Fig. 6: the fine-mode fraction measured by MODIS is 0.5-0.6, indicating that the aerosols are not very small. This is not surprising, for sulphate droplets are highly hygroscopic and grow rapidly in a humid environment. The SCI, in contrast, is most sensitive to small particles with large spectral dependences of AOT.

With this example we have shown that with SCI from GOME-2, SCIAMACHY, and OMI we are able to detect non-absorbing sulphate aerosols. As it is difficult to separate contributions of aerosols from those of clouds or ocean colour, it is recommended to use SCI in combination with AOT from, e.g., MODIS.

4. HICRU

We implemented a prototype version of HICRU for the O3MSAF operational processor. The current GOME-2 prototype implementation is documented in the GOME-2 HICRU ATBD, from which the description of the HICRU algorithm (Section 2) and the validation study with FRESCO+ version 6 (Section 5) are presented below.
The algorithm was developed at the University of Heidelberg (Germany) and the Max Planck Institute for Chemistry in Mainz (Germany) by M. Grzegorski, and is described in [Grzegorski et al., 2006] for GOME and in [Grzegorski, 2009] for both GOME and SCIAMACHY. In the framework of our visiting scientist project, a HICRU prototype was linked to the Opera software at KNMI by O. Tuinder.

4.1. Short description of HICRU

The detection of clouds by passive satellite remote sensing in the UV-visible wavelength range is based on one or several of the following properties of clouds: clouds are bright, clouds are white, and clouds shield the underlying atmosphere and surface from view. The cloud fraction determination algorithm of HICRU makes use of the first property (brightness) by comparing the reflectance of a given scene with a reference minimum reflectance value ("clear scene") and a reference maximum reflectance value ("fully clouded scene"). This procedure is equivalent to the FRESCO+ approach of cloud fraction determination but for three important differences [Koelemeijer et al., 2001; Wang et al., 2008; Grzegorski et al., 2006]:

1. The minimum reflectance value is empirically determined by time-series analysis of the input reflectances in HICRU, whereas for FRESCO+ the reflectance of the "clear" scene is calculated using a radiative transfer model (RTM) and surface albedo input from a database.
2. In the radiative transfer calculation of the maximum reflectance value, the cloud is modelled explicitly with a Henyey-Greenstein phase function (g = 0.85) and a cloud optical thickness (COT) of 50. In FRESCO+, the cloud is approximated by a Lambertian reflector with an albedo equal to 0.8.
3. The scene reflectances are read from one of the instrument's PMD channels, as opposed to the science channels used for determination of cloud fraction by FRESCO+.

The first point is a unique feature of the HICRU algorithm. The most important advantages of the use of a dynamic, empirical map of "clear scene" reflectances are that (a) the algorithm is less sensitive to changes (e.g., degradation) of the input data; (b) seasonal variation can be taken into account; (c) using varying time ranges for the determination of the "clear scene" reflectances, gaps due to persistent cloud cover in short-term (e.g., monthly) maps can be filled up with values from longer-term (e.g., seasonal or yearly) maps. Such minimum-reflectance maps can be based on many years' worth of data (climatologically) or can be determined for each year separately to take degradation or changes in surface reflectance into account. Due to their high reflectivity and the difficulties in distinguishing them from cloudy scenes, ice and snow-covered regions are excluded from the minimum-reflectance maps.
The use of reflectances from a PMD channel, in this case PMD-p 13 (centre wavelength: 639 nm), provides a spatially better resolved product than can be obtained from science channels. For example, the spatial resolution of GOME-2's PMDs is a factor of eight higher

than that of its corresponding science channels. The use of PMD reflectances is possible because the higher spectral resolution of the science channels is not required for the HICRU cloud detection algorithm.

4.2. Validation of HICRU for GOME-2 with FRESCO+

Here we describe the comparison between HICRU and FRESCO+ (version 6) effective cloud fractions for one week's worth of GOME-2 data (July 1-7, 2011, totalling 638,156 data points). FRESCO+ data were obtained from EUMETSAT's GOME-2 Level1 product. In Figure 7 we show cloud fractions determined from a small part of a GOME-2 orbit on July 1, 2011. The left panel displays FRESCO+ cloud fractions at science channel resolution and the right panel shows HICRU cloud fractions at PMD resolution. The spatial agreement between FRESCO+ and HICRU is very good, but FRESCO+ retrieves systematically higher cloud fractions than HICRU. The improvement in spatial resolution from FRESCO+ to HICRU is apparent.

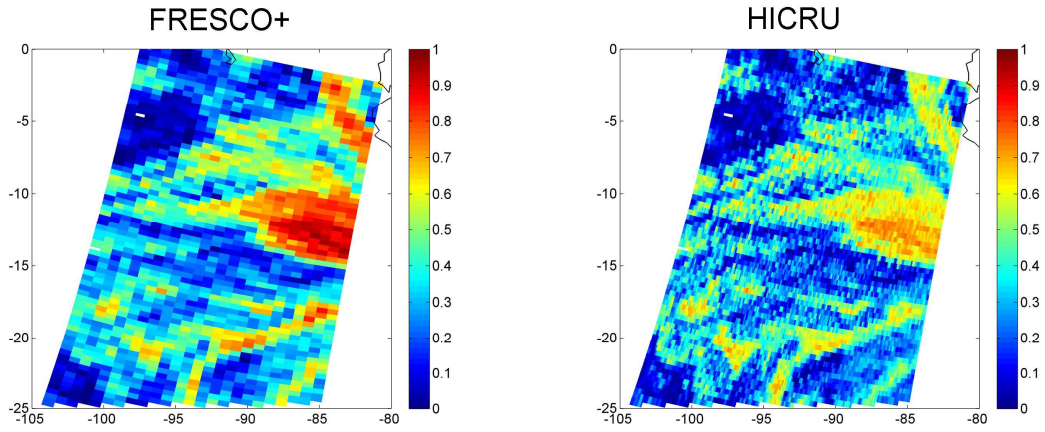

Figure 7. GOME-2 measurements of effective cloud fraction retrieved by FRESCO+ (left) at science channel resolution and by HICRU (right) at PMD resolution. Data were recorded west of the South American continent at 15:24-15:33 UTC on July 1, 2011.

For a more quantitative comparison of cloud fractions, several preparatory steps have to be performed: First, the data need to be collocated. For this verification study, we calculated the simple un-weighted mean of the eight PMD pixels corresponding to one science channel pixel, ignoring the partial overlap of consecutive PMD pixels. By shifting the averaging window by up to three PMD pixels the effect of spatial aliasing was investigated [Tilstra et al., 2011]. The agreement between HICRU and FRESCO+ cloud fractions was found to be slightly better for a PMD shift of zero than for a shift of 1.

Second, the difference in cloud models used for the calculation of the cloud fraction needs to be taken into account. As noted already by Popp and co-workers [Popp et al., 2011], assuming a Lambertian surface with an albedo of 0.8, like in the case of FRESCO+, leads to higher effective cloud fractions than the assumption of a cloud modelled with a Henyey-Greenstein phase function and an optical depth of 50. Not taking this difference into account causes a viewing-angle dependent slope in the correlation plots of HICRU CF_{eff} against FRESCO+ CF_{eff}. This is shown exemplarily in Figure 8 for data with SZA between 40° and 50° and VZA between -35° and -25° (RAZI < 90°, in the west of the swath). In

panel A, HICRU CF_{eff} are plotted against FRESCO+ CF_{eff}; in panel B, the same data are shown, but FRESCO+ CF_{eff} were modified by multiplying with a certain factor to agree with the HICRU cloud definition. This factor is the ratio of CF_{eff} calculated using a model cloud with COT = 50 to CF_{eff} calculated using a model Lambertian cloud with an albedo of 0.8. The modification factor depends on surface albedo and observation geometry. As shown in the plots, the correlation has barely changed (from 0.988 to 0.986), but the slope has improved significantly from 0.79 to 0.94.

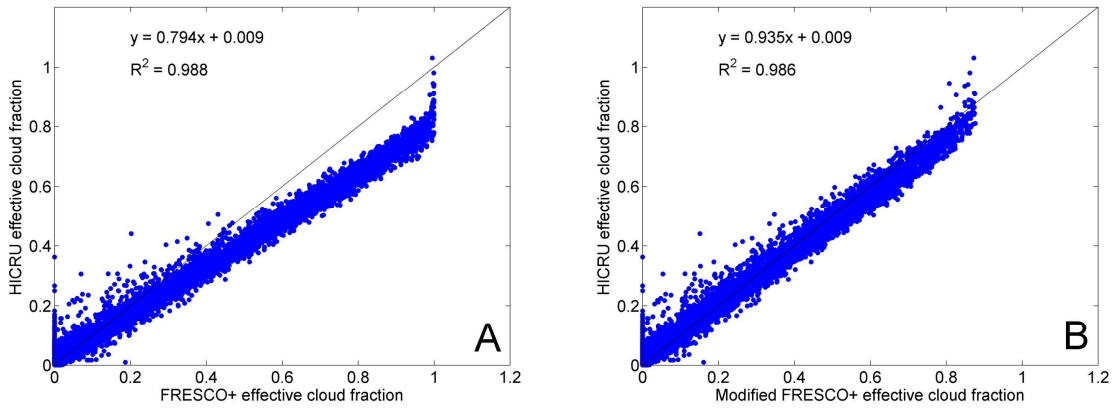

Figure 8. Correlation plots of HICRU CF_{eff} and FRESCO+ CF_{eff} for July 1-7, 2011. Only data with SZA between 40° and 50°, and VZA between -35° and -25° are shown. A, untreated FRESCO+ data; B, FRESCO+ data modified to agree with the HICRU cloud model (see text). The coefficients of a linear fit to the data are shown in the top of the plots, together with the correlation coefficient.

In Figure 9, we show the effective cloud fractions as determined by FRESCO+ and HICRU for July 1, 2011. As in Figure 7, the good agreement between the two products for most of the globe is evident. However, some marked differences are also found that are most clearly seen in the difference plot depicted in the lower right panel. Some of the regions with large differences (of 0.25 or more) are clearly regions with high surface albedo (deserts), for example the Sahara. This indicates effects of the different treatment of surface reflectivity by the two cloud retrieval algorithms. Other regions with strong deviations are more difficult to explain, like the Southeast coast of the USA or Eastern Europe. A more detailed investigation into these regions is required.

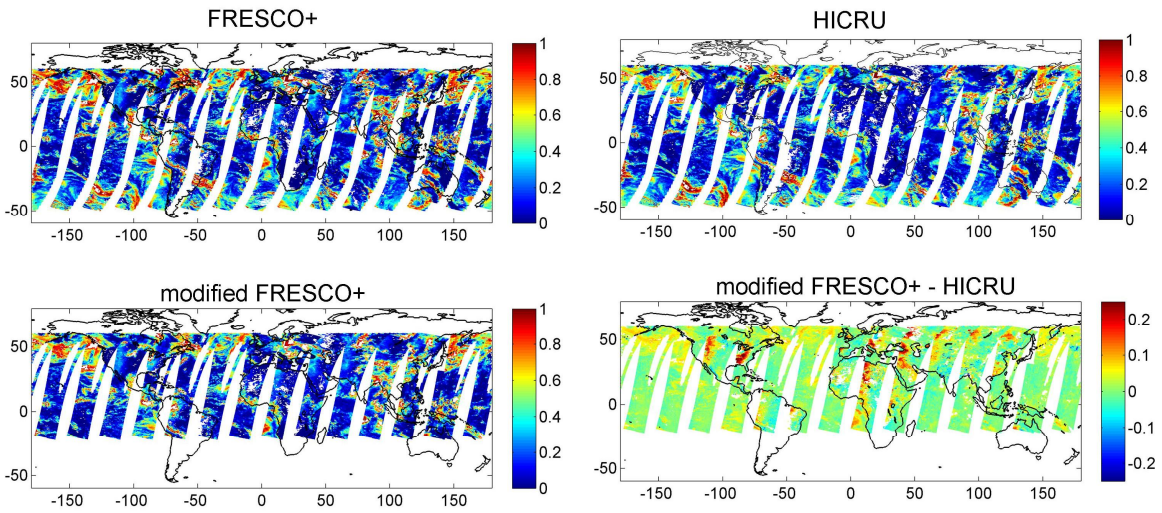

Figure 9. Effective cloud fractions from GOME-2, calculated using the FRESCO+ (top left) and HICRU (top right) algorithms (all at science channel resolution). The lower left panel contains FRESCO+ effective cloud fractions modified to agree with the HICRU cloud model (see text for details). The lower right panel is a difference plot between modified FRESCO+ and HICRU effective cloud fractions. Data are from July 1, 2011; backscans and pixels in sun glint geometry were discarded.

In Tables 1a and 1b, we present the correlation coefficients and the slopes of the linear fit of HICRU CF_{eff} *vs.* FRESCO+ CF_{eff} for various surface types (ocean, dark land and bright land) and for several subsets of solar and viewing geometries. As we expect from two so similar retrieval algorithms, the correlation is generally very high ($R^2 \geq 0.98$), particularly over ocean and dark land surfaces. Due to the differences in treatment of the surface, the agreement between the two algorithms becomes progressively worse with increasing surface albedo, as seen in the fifth column in Table 1a.

Table 1a. Correlation coefficients (R^2) between HICRU CF_{eff} and FRESCO+ CF_{eff} for various subsets of GOME-2 data from July 1-7, 2011. The albedo ranges corresponding to the selected surface types are given in parenthesis in the column heads.

SZA	VZA	Ocean (< 0.05)	Dark land (0.05-0.1)	Bright land (>0.2)
< 60°	< 45°	0.993	0.981	0.925
	< 5°	0.995	0.984	0.966
30°-40°	< 45°	0.993	0.980	0.913
	< 5°	0.995	0.984	0.962
40°-50°	< 45°	0.994	0.984	0.961
	< 5°	0.995	0.986	0.980
50°-60°	< 45°	0.993	0.983	0.971
	< 5°	0.995	0.989	0.972

Table 1b. Slope of the linear fit of HICRU CF_{eff} vs. FRESCO+ CF_{eff} for various subsets of GOME-2 data from July 1-7, 2011. The albedo ranges corresponding to the selected surface types are given in

parenthesis in the column heads. Before fitting, FRESCO+ data were modified to minimize the effect of the differences in cloud models, as described in the text.

SZA	VZA	Ocean (< 0.05)	Dark land (0.05-0.1)	Bright land (>0.2)
< 60°	< 45°	0.921	0.916	0.910
	< 5°	0.917	0.920	0.920
30°-40°	< 45°	0.920	0.923	0.913
	< 5°	0.913	0.925	0.924
40°-50°	< 45°	0.933	0.898	0.910
	< 5°	0.931	0.900	0.914
50°-60°	< 45°	0.902	0.889	0.882
	< 5°	0.904	0.888	0.911

In Table 1b it can be seen that a slope (unequal to 1) between CF_{eff} determined by HICRU or FRESCO+ remains, even after modification of FRESCO+ CF_{eff} to minimize the effect of the differences in cloud models: HICRU cloud fractions are nearly always 8-10% smaller than those determined by FRESCO+. One reason is the remaining differences between the cloud models used in the two algorithms, in particular with respect to the angular dependence of reflectances: the Lambertian cloud model used in FRESCO+ has isotropic reflection properties, whereas HICRU uses a cloud with a pronounced forward-scattering peak (Henyey-Greenstein asymmetry parameter = 0.85). Another explanation could be a difference in radiance calibration for the science channels and PMD channels. However, in the study by Tilstra [2011] the agreement between PMD-13 reflectances and the corresponding science channel reflectances was found to be excellent. Another possible explanation is the partial overlap of the PMD pixels, which leads to a higher weighting of the science channel pixel centre with respect to the sides. Such weighting is, however, expected to lead to a decreased correlation, not to a systematic slope. This issue needs to be addressed in the future.

To conclude, we find excellent – albeit not perfect – agreement between HICRU and FRESCO+, indicating that the implementation of the HICRU prototype for GOME-2 was successful.

5. Conclusions and recommendations

The SCattering Index is a very useful addition to AAI, complimenting the AAI's sensitivity to absorbing aerosols with the ability to detect aerosols that absorb little or no UV radiation. Together, the UV Aerosol Indices (SCI and AAI) provide information on aerosol absorption – data that are not easily obtained by other space-based instruments. This information is even available in the presence of clouds, which is of importance for instruments with coarse spatial resolution (such as GOME-2), where cloud-free measurements are scarce. Although all but a few (very high) UVAI values can be used reliably on an individual measurement basis, we demonstrated the potential of the spatial or temporal average for aerosol characterisation in section 3 in this report. Nevertheless, UVAI, and in particular SCI should be used with caution: we recommend the combination with AOT from, e.g., MODIS or AERONET to ensure that the observed UVAI is caused by aerosols and not by clouds or the surface.

The HICRU effective cloud fraction algorithm has two important advantages: because it is based on PMD reflectances, it has a higher spatial resolution than science-channel-based algorithms (e.g., FRESCO+). And unlike FRESCO+, HICRU does not depend on a surface albedo database for its cloud retrieval, but instead determines clear-sky reflectances by applying image sequence analysis to the dataset itself.
The implementation of a HICRU prototype for GOME-2 at KNMI was successful, although several issues remain to be understood and resolved. We recommend that the mature HICRU algorithm be implemented in the Level-1 product so that it can be used in combination with science channel products, but also with (future) PMD products such as UVAI and AOT.

6. Acknowledgments

MODIS and AERONET data were provided by NASA and were downloaded from the LAADS (ladsweb.nascom.nasa.gov) and the AERONET websites (http://aeronet.gsfc.nasa.gov/). The AERONET PIs and co-workers are thanked for setting up and maintaining the AERONET sites BacGiang, Beijing, Chiang Mai, Mukdahan, Silpakorn, XiangHe, and Xinglong.

7. References

Graaf, M. de, P. Stammes, O. Torres, R. Koelemeijer : Absorbing Aerosol Index : Sensitivity analysis, application to GOME and comparison with TOMS, J. Geophys. Res., 110, D01201, 2005.

Graaf, M. de : Remote sensing of UV-absorbing aerosols using space-borne spectrometers, Ph.D. thesis, Free University, Amsterdam, 2006

Grzegorski, M., M. Wenig, U. Platt, N. Fournier, P. Stammes, T. Wagner: The Heidelberg iterative cloud retrieval utilities (HICRU) and its application to GOME data, Atmos. Chem. Phys., 6, 2006.

Grzegorski, M.: Cloud retrieval from UV/VIS satellite instruments (SCIAMACHY and GOME). Ph.D. thesis, University of Heidelberg, Germany, 2009.

Herman, J. R., P. K. Bhartia, O. Torres, C. Hsu, C. Seftor, and E. A. Celarier: Global distributions of UV-absorbing aerosols from NIMBUS 7/TOMS data, Journal of Geophysical Research, 102(D14), 16,911-16,922, 1997.

Holben, B., T. Eck, I. Slutsker, D. Tanre, J. Buis, A. Setzer, E. Vermote, J. Reagan, Y. Kaufman, T. Nakajima, F. Lavenu, I. Jankoviak, A. Smirnov: AERONET – A federated instrument network and data archive for aerosol characterization, Rem. Sens. Environ., 66, 1-16, 1998.

Koelemeijer, R.B.A., P. Stammes, J.W. Hovenier, J.F. de Haan: A fast method for retrieval of cloud parameters using oxygen A band measurements from GOME, J. Geophys. Res., 106, 3475-3490, 2001.

Penning de Vries, M., S. Beirle, T. Wagner: UV Aerosol Indices from SCIAMACHY: Introducing the SCattering Index (SCI), Atmospheric Chemistry and Physics, 9, 9555-9567, 2009.

Penning de Vries, M., and T. Wagner: Modelled and measured effects of clouds on UV Aerosol Indices on a local, regional, and global scale, Atmospheric Chemistry and Physics, 11, 12715-12735, 2011.

Popp C., P. Wang, D. Brunner, P. Stammes, Y. Zhou, M. Grzegorski: MERIS albedo climatology for FRESCO+ O_2 A-band cloud retrieval, Atmos. Meas. Tech., 4, 463-483, 2011.

Remer, L., R. Kleidman, R. Levy, Y. Kaufman, D. Tanre, S. Mattoo, J. Vanderlei Martins, C. Ichoku, I. Koren, H. Yu, B. Holben: Global aerosol climatology from the MODIS satellite sensors, J. Geophys. Res., 113, L14S07, doi: 10.1029/2007JD009661, 2008.

Tilstra, L.G., O.N.E. Tuinder, P. Stammes: GOME-2 PMD band reflectances verification report. KNMI-RP-2011-01, 2011.
http://o3msaf.fmi.fi/docs/vr/Validation_Report_ARS_AAI_Jan_2012.pdf

Tilstra, L.G., O.N.E. Tuinder, P. Stammes: O3M SAF Validation Report: Absorbing Aerosol Index, SAF/O3M/KNMI/VR/AAI/001, 2012.

Tilstra, L.G., M. de Graaf, I. Aben, P. Stammes: In-flight degradation correction of SCIAMACHY UV reflectances and Absorbing Aerosol Index, J. Geophys. Res., 117, D06209, 2012.

Torres, O., P. K. Bhartia, J. R. Herman, Z. Ahmad, and J. Gleason: Derivation of aerosol properties from satellite measurements of backscattered ultraviolet radiation: Theoretical basis, Journal of Geophysical Research, 103(D14), 17,099-17,110, 1998.

Wang, P., P. Stammes, R. van der A, G. Pinardi, M. van Roozendael: FRESCO+: an improved O_2 A-band cloud retrieval algorithm for tropospheric trace gas retrievals, Atmos. Chem. Phys., 8, 6565-6576, 2008.

8. Abbreviations

AAI	Absorbing Aerosol Index
AERONET	AErosol RObotic NETwork, network of ground-based sun-photometers
ATBD	Algorithm Theoretical Basis Document
CF	Cloud Fraction
FMF	Fine-Mode Fraction
GOME-2	Global Ozone Monitoring Experiment-2, instrument on METOP A
HICRU	HICRU Iterative Cloud Retrieval Utilities
KNMI	Royal Netherlands Meteorological Institute (De Bilt, Netherlands)
MODIS	MODerate resolution Imaging Spectrometer, instruments on TERRA and AQUA
MPIC	Max Planck Institute for Chemistry (Mainz, Germany)
OMI	Ozone Monitoring Instrument, instrument on AURA
PMD	Polarization Measurement Device
SCI	SCattering Index
SCIAMACHY	SCanning Imaging Absorption spectroMeter for Atmospheric CHartographY, instrument on ENVISAT
VS	Visiting Scientist

Appendix 1. Project overview and time schedule

The goal of the project was to implement the SCI, in addition to the existing AAI, for GOME-2, subsequent verification of SCI with ground-based aerosol data from AERONET [Holben et al., 1998] and MODIS aerosol optical thickness data, and comparison with Aerosol Indices from SCIAMACHY and OMI. A new algorithm for cloud retrieval using GOME-2 PMDs was implemented to augment the Aerosol Indices with cloud fractions and cloud heterogeneity.

Table 2. Overview of the project tasks for the Visiting Scientist (VS). Abbreviations: GT, Gijsbert Tilstra; OT, Olaf Tuinder; MG, Michael Grzegorski; MPdV, Marloes Penning de Vries. The tasks of the VS are divided into four work packages (WP). The column labelled "duration" refers to the time that was invested by the VS.

Phase	Task	Scientist(s)	Duration
Preparation	GOME-2 L1 degradation correction	GT – KNMI	
WP1 – GOME-2 Cloud retrieval			**1 month**
	Modification of HICRU cloud retrieval for GOME-2	MPdV (VS) MG – MPIC	1 month
WP2 - Implementation			**10 weeks**
	Implementation of SCI for GOME-2	MPdV (VS) GT, OT – KNMI	<<1 week
	Implementation of HICRU for GOME-2	MPdV (VS) OT – KNMI MG – MPIC	10 weeks
WP3 - Verification			**10 weeks**
	Verification of HICRU (with FRESCO+)	MPdV (VS)	5 weeks
	Verification of SCI (AERONET and MODIS)	MPdV (VS)	5 weeks
WP4 - Comparison			**1 month**
	Comparison with SCIAMACHY and OMI Aerosol Index	MPdV (VS)	<1 month
	Writing of reports	MPdV (VS)	<1 month

Preparatory work was done at KNMI in collaboration with the MPIC. In particular, this concerned the cloud retrieval, which had to be modified for use with GOME-2 by MPIC and then implemented at KNMI. The work assigned to the visiting scientist was divided into four work packages:

1. modification of the HICRU cloud retrieval algorithm for GOME-2;
2. implementation of SCI and the cloud retrieval algorithm;
3. verification of GOME-2 Aerosol Indices and of the new cloud product;

4. comparison of GOME-2 Aerosol Indices with Aerosol Indices from SCIAMACHY and OMI.

Work package 4 also includes the writing of a HICRU-prototype algorithm document, the adaptation of the GOME-2 aerosol product algorithm document to include SCI, and the writing of the final report.

In Table 2, an overview of the project is shown.

The results from the project are presented in this final report and will be published in a scientific journal. The deliverables are:

- algorithm description for the HICRU-type cloud retrieval for GOME-2;
- a new section on SCI in the GOME-2 Aerosol ATBD;
- this final report.

The total duration of the project was 7 months (28 weeks) of full-time work; the work was spread over 21 months and was carried out partly at KNMI and partly at MPIC. A time plan of the project is outlined in Table 3. The project (excluding the preparatory phase) took place between June 2010 and February 2012.

Table 3. Realized time schedule for the project of the visiting scientist. The project has been partially executed at KNMI, and partly at MPIC. The indicated phases are explained in more detail in Table 2.

Phase (see Table 2)	Month	# weeks at KNMI	# weeks at MPIC
WP 1 – GOME-2 Cloud retrieval	June 2010	1 week	1 week
	July 2010	1 week	1 week
WP 2 - Implementation	August 2010	1 week	1 weeks
	September 2010	1 week	2 weeks[1]
	October 2010	1 week	1 week
	November 2010	0 weeks	1 week
	December 2010	0 weeks	0 weeks
	January 2011	2 weeks	1 week
WP 3 - Verification	February 2011	1 week	1 week
	March 2011	2 weeks	1 week
	October 2011	0 weeks	1 week
	November 2011	1 week	1 week
	December 2011	1 week	1 week
WP4 - Comparison	January 2012	1 week	1 week
	February 2012	1 week	1 week
	Total	**14 weeks**	**14 weeks**

[1] *Including 1 week at the EUMETSAT Meteorological Satellite Conference to report on the progress of the project*